Microearthquake seismicity of the Mid-Atlantic Ridge at 5°S: A view of tectonic extension

Frederik Tilmann[1]
GEOMAR, Kiel, Germany

Ernst Flueh, Lars Planert, Tim Reston, and Wilhelm Weinrebe
Leibniz-Institut fur Meereswissenschaften an der Universität Kiel (IFM-GEOMAR), Kiel, Germany

Received 6 October 2003; revised 19 March 2004; accepted 10 May 2004; published 23 June 2004.

[1] We report measurements made with an ocean bottom array which was operated for 10 days on the Mid-Atlantic Ridge just south of the 5°S transform fault/fracture zone. A total of 148 locatable earthquakes with magnitudes ~0.5–2.8 were recorded; seismic activity appears to be concentrated within the western half of the median valley. The median valley seismic zone is bounded in along-axis direction by the transform fault to the north and the tip of the axial volcanic ridge to the south. A few scattered events occurred within the inside corner high, on the transform fault, and in the western sidewall close to the segment center. Earthquakes reach a maximum depth of 8 km below the median valley floor and appear to be predominantly in the mantle, although a few crustal earthquakes also occurred. The presence of earthquakes in the mantle indicates that it is not strongly serpentinized. We infer the median valley seismic activity to primarily arise from normal faulting. *INDEX TERMS:* 7230 Seismology: Seismicity and seismotectonics; 7220 Seismology: Oceanic crust; 3035 Marine Geology and Geophysics: Midocean ridge processes; 3025 Marine Geology and Geophysics: Marine seismics (0935); *KEYWORDS:* earthquake location, Mid-Atlantic Ridge, tectonic extension

Citation: Tilmann, F., E. Flueh, L. Planert, T. Reston, and W. Weinrebe (2004), Microearthquake seismicity of the Mid-Atlantic Ridge at 5°S: A view of tectonic extension, *J. Geophys. Res.*, *109*, B06102, doi:10.1029/2003JB002827.

1. Introduction

[2] Magmatism and mechanical extension are processes contributing to seafloor spreading. Whereas magmatic injection is dominant for fast spreading ridges, mechanical extension is likely to be important in slow spreading ridges [*Mutter and Karson*, 1992]. Evidence for the strong role of mechanical extension at slow spreading ridges can be seen in the morphology of the spreading axis (well-developed median valleys with at least one bounding sidewall with strong relief), the intermittent nature of magmatic activity (no continuous eruption centers are generally discernible, and seismically detectable magma chambers, common at fast spreading ridges, are usually absent), the higher rate and larger depth extent of seismic activity (both in local surveys [e.g., *Toomey et al.*, 1988] and globally [*Huang and Solomon*, 1988; *Rundquist and Sobolev*, 2002]), and the strong segmentation by transform faults and nontransform ridge discontinuities (NTD). A strong asymmetry along both types of segment boundary is frequently observed, with the inside corner next to the active transform or NTD being characterized by high topography, large inferred fault spacings, and a positive mantle Bouguer gravity anomaly indicative of thinned crust, and the outside corner next to the inactive fracture zone being associated with more subdued topography, small inferred faults spacings, and a negative gravity anomaly [*Shaw and Lin*, 1993; *Escartín and Lin*, 1995]. This asymmetry, combined with the observation of corrugations parallel to the spreading direction on many inside corner highs (ICH) and the recovery of gabbro and serpentinite samples from their surface, has led to a model where ICHs are interpreted to be the unroofed footwalls of deeply penetrating detachment faults and extension is thus largely accommodated by simple shear [*Tucholke and Lin*, 1994].

[3] Successor faults might then develop in the ICH to accommodate bending as result of progressive footwall rotation. In this model the outside corner is characterized by high-angle, small-offset normal faulting between rotated fault blocks.

[4] Toward the segment center, where fault spacing is usually small and the across-axis profile is more symmetric [*Shaw and Lin*, 1993], the detachment is thought to die out because of thermal structure or as a geometric requirement. The geometric requirement only applies to segments where the transform or NTD steps in the same direction at both ends; an inside corner is thus paired with an outside corner, and the segment center needs to mediate between the different structures. Being farther away from the cooling influence of the transform or NTD, the segment centers are likely to be warmer, and the lithosphere is accordingly weaker. The median valley within segment centers is often

[1] Also at Bullard Laboratories, Department of Earth Sciences, University of Cambridge, Cambridge, UK.

0148-0227/04/2003JB002827$09.00

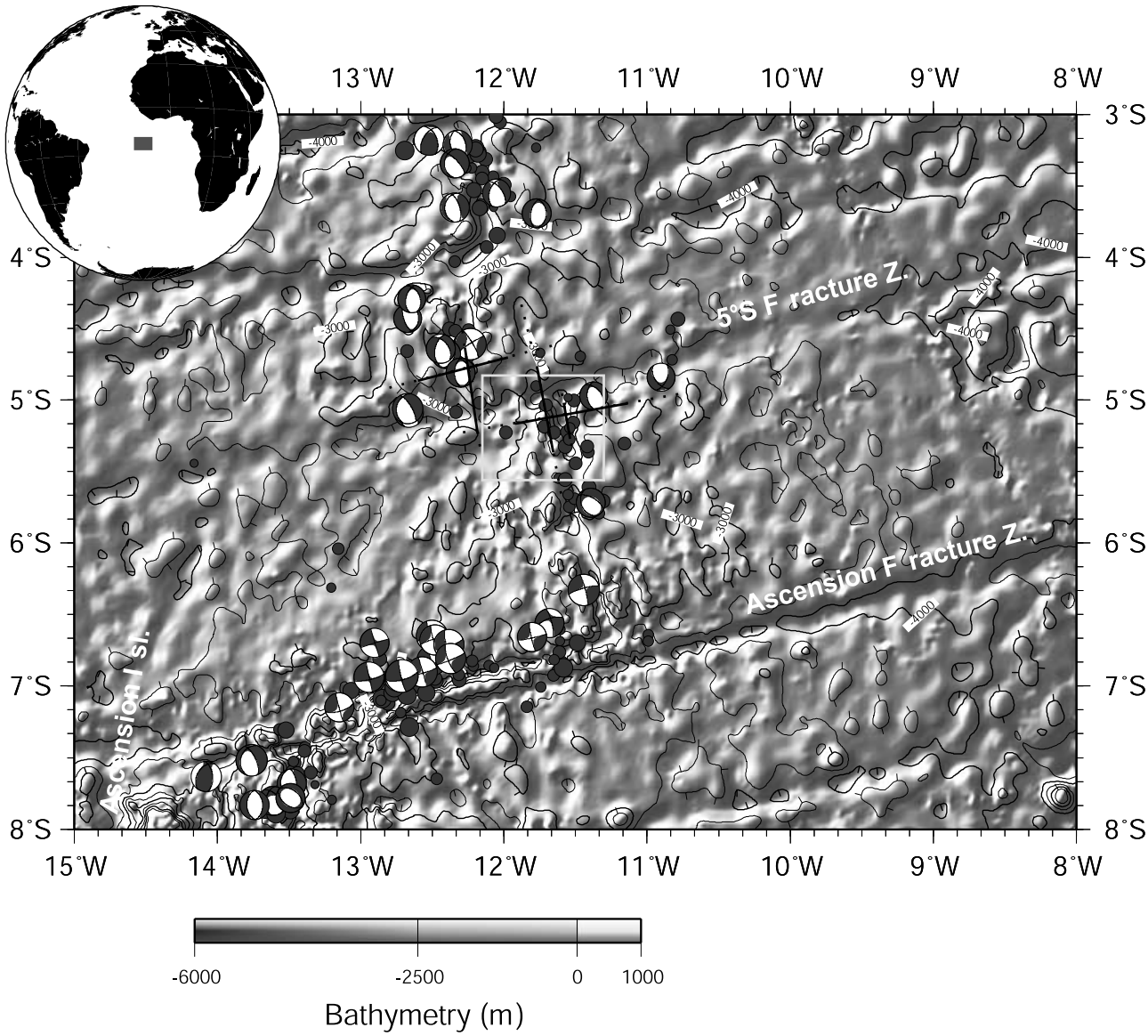

Figure 1. Regional map of a part of the southern Mid-Atlantic Ridge including the study area. Several segments of the Mid-Atlantic Ridge, which trend NNW-SSE, are offset by minor transform faults. The rectangle marks the location of the detailed map in Figure 2. Circles indicate earthquakes from 1963 to 2001 in the EHB catalog [*Engdahl et al.*, 1998]. Harvard CMT solutions until June 2003 [*Dziewonski et al.*, 1981] are shown, where the double-couple part of the moment tensor is indicated by black lines. As all events in this area are likely to be close to double couple, the deviations of the moment tensors from a double couple are a coarse indicator of the uncertainty of the solution. Bathymetry is derived from satellite altimetry [*Smith and Sandwell*, 1997]; contours are drawn at 500 m intervals. The lines indicate the position of refraction profiles collected during the experiment; the continuous part shows the coverage of profile stations, and the dotted part shows the range for shooting.

elevated by 1000 m or more compared to the median valley near the segment boundaries, presumably because of increased crustal thickness near the center, which in turn is related to the higher temperatures just discussed [see, e.g., *Neumann and Forsyth*, 1993].

[5] Seismicity patterns can provide a direct image of the tectonic processes currently operating and give indirect information about the temperature through the depth of the brittle-ductile transition. Here we report on the microearthquake activity of the Mid-Atlantic Ridge segment just south of 5°S on the basis of a brief survey carried out as part of R/V *Meteor* cruise M47/2 in 2000, also drawing on several wide-angle profiles shot in the area [*Planert et al.*, 2003]. The segment is bounded to the north by the 70 km long left-laterally stepping 5°S transform fault and fracture zone (Figure 1).

[6] The study area is unusual in that the ICH elevation is almost matched by that of the outside corner massif, albeit the latter is of much smaller lateral extent (Figure 2). This peculiarity and a number of other morphological features

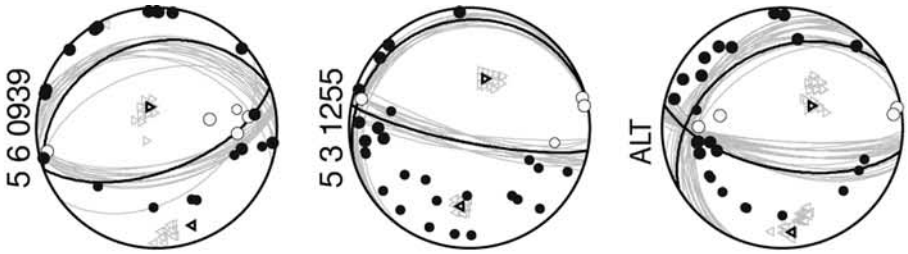
5 6 0939
5 3 1255
ALT

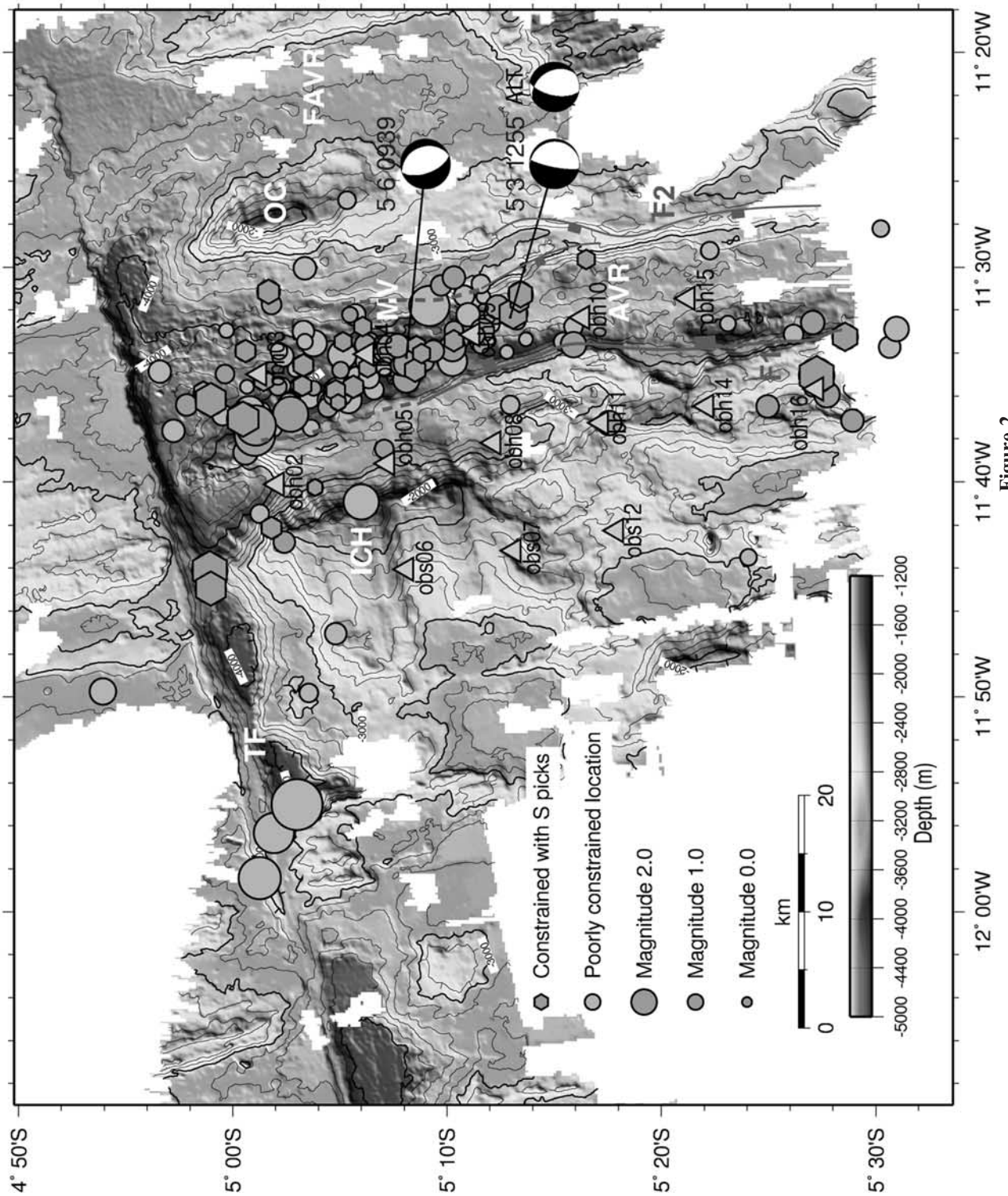
11° 20'W
11° 30'W
11° 40'W
11° 50'W
12° 00'W
4° 50'S
5° 00'S
5° 10'S
5° 20'S
5° 30'S
OC
FAVR
MV
AVR
F2
ICH
TF
5 6 0939
5 3 1255
ALT
obh02
obh03
obh04
obh05
obh06
obh08
obh10
obh11
obh14
obh15
obh16
obs06
obs07
obs12
Constrained with S picks
Poorly constrained location
Magnitude 2.0
Magnitude 1.0
Magnitude 0.0
km
0
10
20
Depth (m)
-5000 -4400 -4000 -3600 -3200 -2800 -2400 -2000 -1600 -1200

Figure 2

have led *Reston et al.* [2002] to propose that the outside corner massif is really part of a fossil ICH which was split by a ridge jump to the west at ~0.75 Ma.

[7] In spite of this peculiarity, we will argue that in fact the seismicity patterns are broadly consistent with previous surveys along the Mid-Atlantic Ridge (MAR) and can be understood in terms of a variation of the basic *Tucholke and Lin* [1994] model: The seismicity suggests that normal faulting is active beneath the western half of the median valley. The currently active faults are not related to the formation of the corrugations on the domal massif but rather represent a more recent phase in the evolution of the segment.

2. Earthquake Location

2.1. Data

[8] A network of altogether 16 free fall ocean bottom stations (consisting of 13 ocean bottom hydrophones (OBH) and three ocean bottom seismometers/hydrophones (OBS)) was deployed on 3 May 2000 on the inside corner high and the median valley in the study area (Figure 2). The array was continuously recording at 100 Hz sampling frequency, while other geophysical and geological investigations (bathymetric mapping, dredging, refraction seismology) were carried out in the study area. The total recording period was 10 days; however, three instruments returned no usable data because of equipment problems, and a number of stations recorded only for a few days, mainly because they were recovered before the end of the experiment in order to be used in the contemporaneous refraction experiments. Because of the rough topography and lack of sedimentary cover at the ridge the seismometers did not couple well to the seafloor, resulting in ringing and delayed signal onsets, such that few usable velocity seismograms were obtained. The hydrophones were partly differential pressure gauges (DPG) and partly piezoelectric hydrophones. They generally produced clear signal onsets for *P* waves and even recorded waves converted from *S* to *P* at the seafloor for some events and stations (Figure 3). Accordingly, most subsequent analysis was based on the hydrophone and DPG recordings. An exception to this rule is station obs12, which recorded reasonable *Z* component seismograms but no usable hydrophone data. Hydrophone records can constrain secondary arrivals other than *S* which are easily confused with *S*. For this reason we verified that similar locations were obtained without using those *S* arrivals.

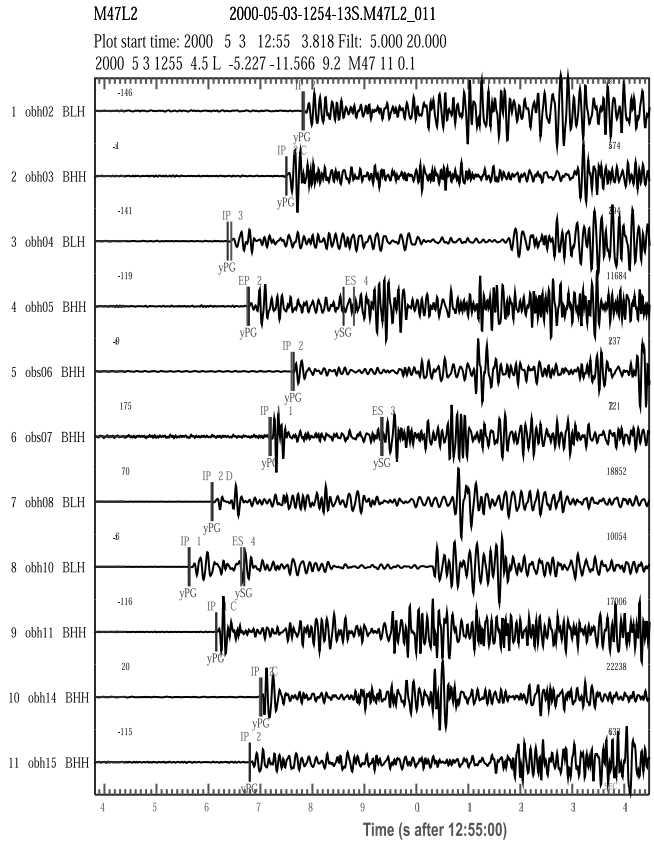

Figure 3. Traces for hydrophone and DPG channels of all stations for the 3 May 2000 1255:04 UT event, filtered with a 5–20 Hz band pass. Analyst picks are marked with phase (black vertical line), and calculated travel times for the inferred location are marked with prefix "y" (gray vertical line) Picks with the number 4 next to them are considered unreliable and were not used in the location procedure. The large arrival appearing 3–5 s after the first arrival is the first stationside multiple in the water column; that is, the delay is proportional to the water depth near the station.

[9] In spite of the short recording time a large number of events were recorded. Basic processing involved the following steps:

[10] 1. Correct the timing of the records assuming linear drift of the data logger clock between synchronization with GPS time at the beginning and end of the experiment.

Figure 2. Distribution of earthquakes recorded with the ocean bottom stations. Red circles and hexagons are events located with at least five stations and azimuthal gap <300°; hexagons indicates at least one *S* arrival was used. Gray circles are marginally located events not fulfilling above criteria. Gray triangles are station locations. Composite focal mechanisms for two groups of events are shown as lower hemisphere projections. For event 5 3 1255 an alternative solution (labeled ALT), which results from the use of a different velocity model, is also shown. Details of the focal mechanism solutions are shown to the right of the map, where the thick black line shows the preferred solution (identical to the mechanisms shown in the map), the thin gray lines indicate other solutions that are consistent with the data, and black and white circles show compressive and dilatational first motion, respectively. Direct rays leaving the earthquake focus in upward direction are plotted at the opposite azimuth, and the incidence angle is set to the angle between the ray direction and vertical up. Triangles indicate possible *P* and *T* axes. The bathymetry is based on processed multibeam soundings acquired during the cruise. Marked morphological features: MV, Median Valley; TF, transform fault; ICH, inside corner high; OC, outside corner massif; AVR, axial volcanic ridge; FAVR, extinct (fossil) axial volcanic ridge. Faults F1 and F2 were identified by [*Reston et al.*, 2002]. The dashed lines show possible continuations of the faults where their morphological expression is less clear. See color version of this figure at the back of this issue.

[11] 2. Relocate stations using the water wave arrival time of air gun shots.

[12] 3. Band-pass filter with a 5–20 Hz passband. The filtering is crucial for the DPG records, for which otherwise microseismic noise completely obscures the signal. We checked with hydrophone records that signal distortion is minor and that any delay introduced by the filter is not significant.

[13] 4. Generate a preliminary list of events with a trigger algorithm that detects nearly coincident changes in the amplitude at several stations and can detect and remove man-made air gun shots, which otherwise lead to a large number of spurious triggers.

[14] 5. Manually inspect all trigger events and pick arrivals, assigning a weight to each pick. Remove events, which are unclear, presumably not earthquakes, or cannot be picked on at least three stations.

[15] 6. Obtain a preliminary location of each event by linearized inversion and using a one-dimensional (1-D) velocity model derived from the refraction data (see *Planert et al.* [2003] and section 5).

[16] Altogether 148 events were pickable on at least three instruments. Of these, 77 have picks on at least five stations and an azimuthal gap of less than 300° and are referred to as "restricted event set." The remaining 71 events are termed "marginal events." (An azimuthal gap of 300° is not normally considered to be sufficient for a well-constrained location; however, extensive testing of the robustness of these locations with respect to random errors and the assumed velocity models showed that they are well enough located to provide meaningful tectonic information, and should therefore be included.) Twenty-eight events in the restricted data set have at least one *S* pick, and 52 events have reasonably well constrained depth (see Figure 5 caption for further details).

2.2. Method

[17] We relocated all events in the restricted event set at the same time as determining station corrections and the minimum 1-D model, i.e., the model which achieves the best fit of the travel times (using VELEST [*Kissling et al.*, 1994]). Since the event set is rather small and most events fall into the 7–11 km depth band (below sea level), the minimum 1-D model is poorly resolved, and only the average sub-Moho velocity, which is almost 8 km/s, is constrained by the inversion. We considered two extreme models, one appropriate for the median valley, where as we will see, most earthquakes are located, and one appropriate for the ICH, where most stations are located (see Figure 4 for the velocity models). We also relocated the events keeping the model fixed, i.e., by a simple joint hypocenter determination. All inversions achieve a satisfactory fit of the data. We chose the minimum 1-D model resulting from an inversion with the ICH starting model as the preferred model because it yielded the lowest residual RMS. In most instances the systematic differences in inferred location between the different velocity models are small, such that the patterns reported in the following are not affected by the choice of velocity model (see Figures A5–A7 in auxiliary material[1]).

[1]Auxiliary material is available at ftp://ftp.agu.org/apend/jb/2003JB002827.

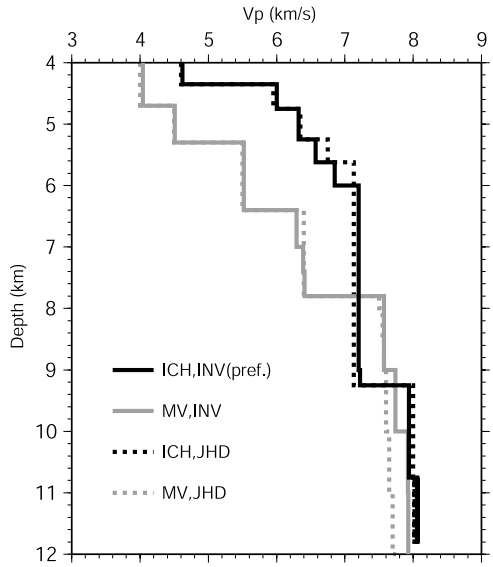

Figure 4. Velocity models used for earthquake location. Models marked INV resulted from a joint inversion for earthquake locations and the velocity model. Models marked JHD are derived from the refraction profiles and are used for joint hypocenter determination.

However, the apparent depth of shallow median valley earthquakes is increased by ~1 km in the median valley model compared to their location in the preferred model.

[18] The picking error was estimated a posteriori by the method of *Wilcock and Toomey* [1991], modified to allow for different pick weights, to be 0.04 s for the highest-quality picks, and 0.08 s for the lowest-quality picks. The location uncertainty due to picking errors is evaluated using a Monte Carlo method, and again all results reported in the following are robust with respect to likely mislocations (Figures A3 and A4 in auxiliary material). Subsequently, we relocated all marginal events with the station terms and, where applicable, the velocity model derived from the restricted data set.

[19] We further relocated the events using the double-difference method [*Waldhauser and Ellsworth*, 2000], trying both an inversion using manual picks only and an inversion using a combination of manual and cross-correlation picks. Whereas the results were broadly consistent with the joint hypocenter or minimum 1-D model locations, they did not concentrate seismicity in narrower bands, and relative relocation vectors between the double-difference method and the conventional techniques showed no systematic pattern. A failure of the double-difference method to improve location accuracy in this experiment would not be surprising because of the relatively small number of picks available for most events. In the absence of further information we thus preferred the locations obtained by the use of absolute travel times.

2.3. Results

[20] The distribution of events is shown in Figure 2. All events with both upper and lower 68% confidence bounds on depth of <2 km are included in the cross sections and maps with gray scale-coded earthquake depth in Figures 5

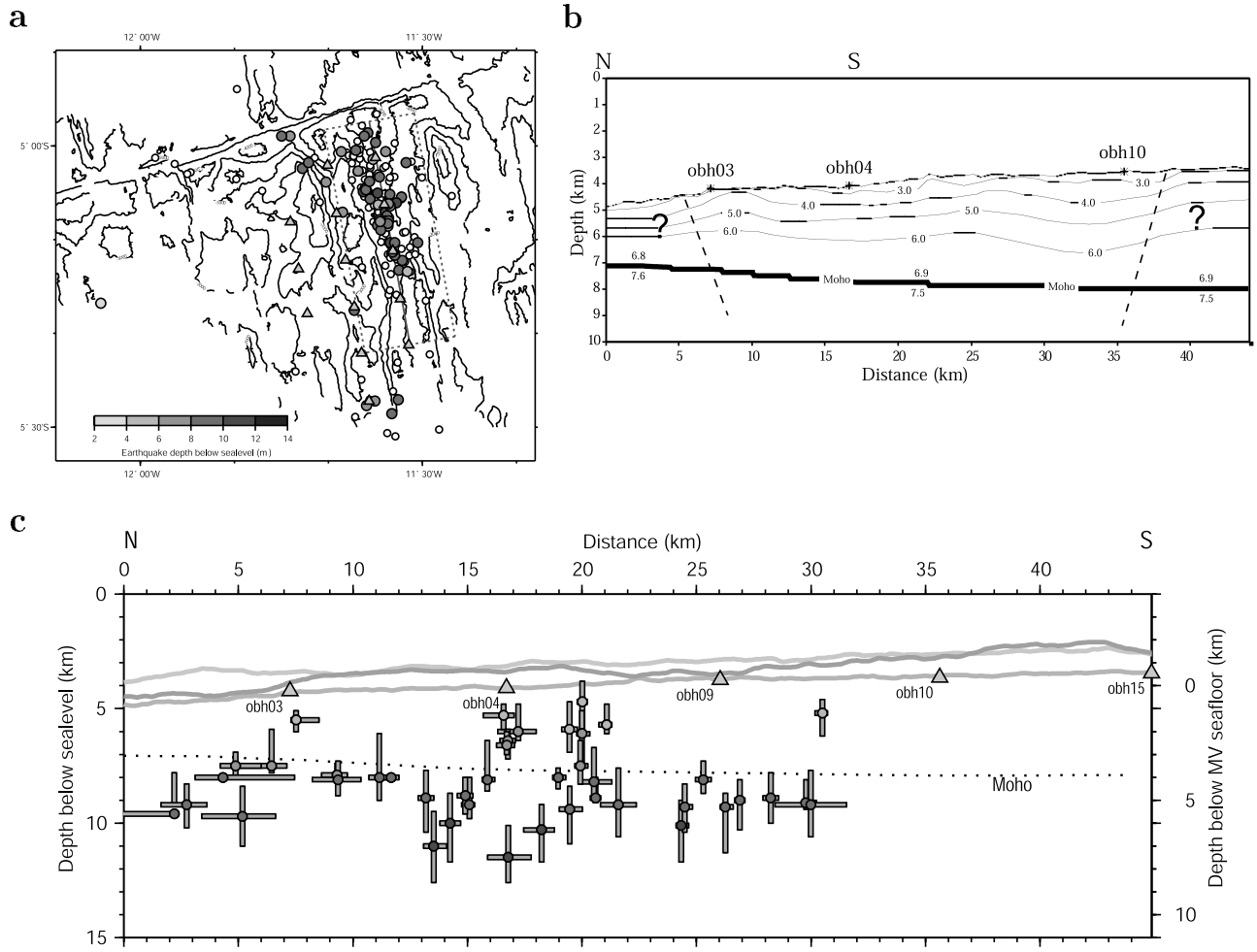

Figure 5. Depth distribution of earthquakes and velocity structure along the median valley. (a) Overview map. Gray circles correspond to events with reasonable depth control (neither upper nor lower 68% confidence bound must be more than 2 km from the optimum solution depth). Open circles correspond to events with poor depth control. The solid line indicates the position of the profiles in Figures 5b and 5c, and the dashed line indicates the size of the box within which earthquakes are projected onto the profile line. (b) *P* velocity model for the median valley based on refraction data. Velocities in the lower crust are poorly controlled and trade off somewhat with velocities in the mantle. The model shown represents a minimum estimate for sub-Moho velocities, but faster sub-Moho velocities (up to 7.7–7.8 km/s) are possible if correspondingly lower crustal velocities are assumed. (c) Cross section along the median valley for all events with reasonable depth control (gray circles in Figure 5a). The shading of circles indicates depth equivalent to Figure 5a. Error bars show 68% confidence bounds in depth and longitude determined by a Monte Carlo method (hence the bounds are not necessarily symmetric). Gray solid lines show the bathymetry (light gray, eastern flank; medium gray, median valley; dark gray, western flank). The bathymetry is taken along the solid and dashed lines in Figure 5a. The Moho depth is from the refraction model in Figure 5b. See enhanced version of this figure in the HTML.

and 6. Traditionally, it is assumed that the availability of *S* picks is critical for earthquake depths to be constrained, whereas we only have *S* picks available for a subset of those events. However, for many events both direct and indirect arrivals have been recorded at different stations. Because these arrivals are associated with rays leaving the focus in upward and downward direction, respectively, the partial derivatives of their arrivals times with respect to depth have opposite signs, and depth can thus be reasonably well constrained even in the absence of *S* waves. It has to be kept in mind that the seismic activity patterns described in the following strictly apply only to the duration of the experiment. Only the events in the median valley are sufficiently numerous and well constrained to warrant a detailed discussion. We will thus defer discussion of these events to later sections but briefly discuss the other groups here.

2.3.1. Median Valley, Along-Axis Deep

[21] The vast majority of events during the experiment occurred within the median valley, referred to henceforward as the median valley seismic zone (MVSZ). Earthquakes are concentrated within a 5–8 km wide zone bounded to the

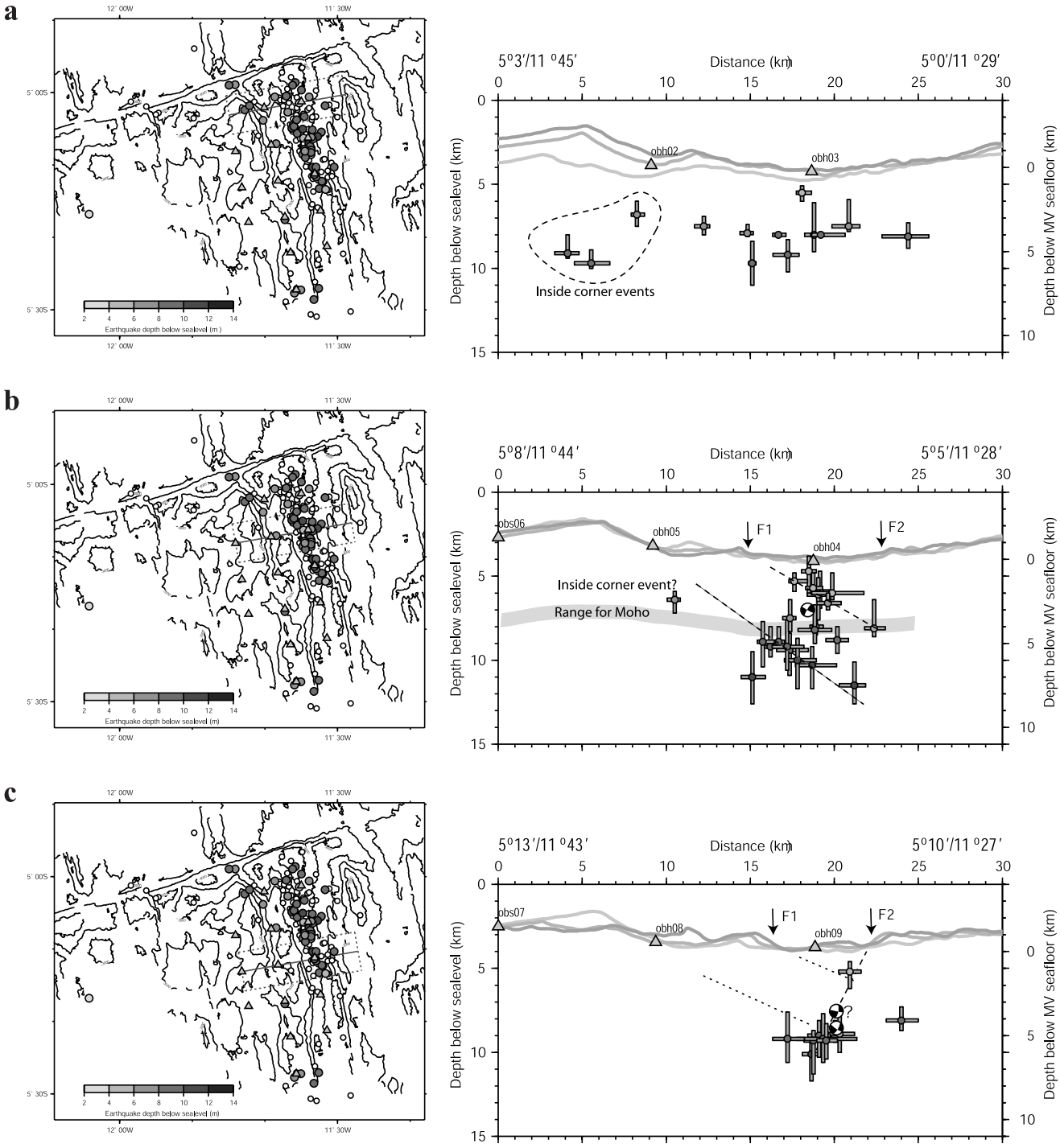

Figure 6. Cross sections perpendicular to the median valley along three adjacent transects. Format is as in Figure 5 except that the light gray bathymetry corresponds to the northern dashed line in map view, the medium gray bathymetry corresponds to the central solid line, and the dark gray bathymetry corresponds to the southern dashed line. (a) Northern profile and (b and c) central and southern profiles, which include a half-sphere-behind-vertical-plane projection of the composite focal solutions 5 6 0939 and 5 3 1255, respectively. As the focal mechanisms are composite solutions, their position in the cross section is approximate, and they are included for visualization of the dip of the focal planes only. Two alternative solutions, between which the data cannot discriminate, are plotted on top of each other for event 5 3 1255 (see text and caption of Figure 2 for further details) in the southernmost cross section. Positions of fault traces F1 and F2 are marked (see Figure 2). Proposed faults are suggested by dashed lines; in Figure 6b, two alternative possibilities are given (see text). The Moho in Figure 6c is derived from a ridge-perpendicular profile. It is less well defined than in Figure 5 because no clear P_mP arrivals were recorded for this profile. See enhanced version of this figure in the HTML.

Table 1. Composite Focal Mechanism Solutions[a]

Composite Solution	Plane 1			Plane 2			Number of Events	Number of Polarities	Polarity Errors
	Strike, deg	Dip, deg	Rake, deg	Strike, deg	Dip, deg	Rake, deg			
5 6 0939[b]	340	30	−90	160	60	−90	5	25	1
5 3 1255, solution 1	344 ± 10	11 ± 5	−116 ± 5	191	80	−85	6	29	0
5 3 1255, solution 2	328 ± 10	36 ± 15	−126 ± 10	191	62	−67	6	29	2

[a]Polarity errors for all three solutions are close to nodal planes (see Figure 2).
[b]Solutions with strikes 340–10° are compatible with the data; 340° was chosen as the strike of the preferred solution because it is parallel to the structure in the topography. The dip is constrained to lie between 25° and 40°, and the rake can lie between −70° and −90° (with the lower bound only obtained for strikes close to 0°).

west by a fault, labeled F1 in Figure 2, which was previously identified from the bathymetric data [*Reston et al.*, 2002].

[22] To the north the seismic zone is bounded by the transform fault; an apparent reduction of activity within 5 km of the transform is not robust when considering the location uncertainties of the earthquakes and the station distribution. To the south the seismic zone terminates rather sharply near the northern tip of the axial volcanic ridge at 5°14′S. The latitude of earthquakes, and thus the limit of the seismic zone, near the southern tip is rather well constrained. We further tested the influence of the station distribution on this limit by relocating all events but removing a number of stations a time. Even when leaving out stations obs12, obh11, and obh10 (the southernmost row) the southern limit of the MVSZ does not change. The eastern limit of the seismically active zone is somewhat less well defined. North of 5°10′S, most earthquakes are in the western half of the valley with a few events near the eastern flank. South of 5°10′S, earthquakes occur under the whole width of the median valley. Earthquakes depths lie between 5 and 12 km below sea level, or equivalently 1–8 km below the median valley floor. The pattern of activity is virtually identical for the restricted and marginal event set, which gives reassurance that no significant bias was introduced by the selection criteria. The two marginal events underneath the outside corner have uncertainties large enough that they might have occurred in the outer reaches of the median valley. Hence we do not consider the outside corner as a separate seismically active zone.

2.3.2. Inside Corner High

[23] A small number of events occurred underneath the ICH. The four events with depth control have depths between 7 and 10 km below sea level, or equivalently 4–8 km below the seafloor, putting them in the mantle and lower crust (see Figures 6a and 6b).

[24] A microearthquake survey of a seismically much more active ICH (at 29°N [*Wolfe et al.*, 1995]) has also placed ICH events in the mantle. *Wolfe et al.* [1995] interpreted the ICH seismicity to result from tectonic extension within a diffuse zone underneath the ICH with no single dominant detachment fault. Analogously, we propose that the few events in the ICH accommodate tensile stresses within the ICH, although we have no focal solution to ascertain the validity of this statement. In any case, the low level of seismic activity, if indeed representative, argues that extension within the ICH is minor compared to the processes operating underneath the median valley.

2.3.3. Western Flank, Close to Segment Center

[25] A cluster near the southernmost station obh16 comprises six events in the restricted set and three marginal events. The four earthquakes with well-constrained depths lie between 6 and 10 km below sea level on an eastward dipping plane (∼30° dip), but the number of events is too small to identify this plane with a fault plane.

2.3.4. Transform Fault

[26] A number of events are likely to have originated on the transform fault. These include the two events in the restricted set just north of the ICH Eastern scarp with depths of 8 and 10 km below sea level and the three large marginal events near 5°02′S, 11°57′W, the uncertainties of which are all consistent with an origin on the transform. In fact, it is remarkable how close to the transform they locate in spite of the considerable distance from the network. The only event that locates north of the transform is particularly poorly constrained, such that it could also have originated on the transform.

3. Focal Mechanisms

[27] First motion polarities were determined on the unfiltered records, if possible. However, it was necessary to apply a 1–20 Hz band-pass filter to the DPG data for all but the largest events in order to make the signal visible above the microseismic noise. As the application of this particular band pass did not change first motion polarities of those arrivals which could be picked on the unfiltered records, we are confident that our results are not biased by the use of the band-pass filter. No individual event provided enough measurements to constrain the focal solution with any degree of confidence. Nevertheless, some systematic trends were discernible: Allowable pressure axes are either close to vertical or their horizontal component is approximately aligned with the median valley direction, and allowable tension axes were in general within ∼30° of the horizontal direction. Assuming double-couple mechanisms, composite focal solutions were then determined for groups of closely spaced events with similar waveforms. Independent and stable solutions could be obtained for only two groups of events (Table 1 and Figure 2) because most of the events occurred at the edge of the array and because takeoff angles are strongly model-dependent at close distances.

[28] The solution for the group of five events within the center of the MVSZ exhibits eastward dipping low-angle normal faulting (or westward dipping high-angle faulting) with a strike parallel to the strike of the median valley bounding fault F1 (340°) or perpendicular to the spreading direction (347° in the NUVEL-1 model [*DeMets et al.*, 1990]); uncertainties are too large to discriminate between both possibilities. The same solution is obtained for both end-member velocity models, i.e., the median valley and the ICH velocity models.

[29] The solution for the group of six events near the southern end of the MVSZ shows some model dependence, and two alternative, albeit similar solutions are presented (Figure 2). The first is obtained for the median valley velocity model and shows extremely low angle normal faulting (<10° eastward dip) or extremely high-angle faulting verging on a dip-slip mechanism, striking 10°, i.e., rotated clockwise from the strike of the solution for the first event group but almost parallel to the southward continuation of bounding fault F1, which exhibits a kink near 5°16′S, a few kilometers south of the event group. The second solution is obtained for the ICH model and shows oblique normal faulting, again with a strike closer to perpendicular to the spreading direction (350°) but still rotated clockwise with respect to the solution to the first event.

4. Earthquake Magnitude

[30] The absolute calibration of our hydrophones was not well determined, and we were also concerned about possible site effects due to the rough topography. Therefore we did not determine seismic moments directly but instead measured peak-to-peak amplitudes within 15 s of the first arrival for each station on the 5–20 Hz band-pass filtered, but not instrument-corrected records; that is, the unit of the amplitude measurements is counts. We then assumed these measurements can be described by (modified from *Hutton and Boore* [1987])

$$M_i = \log_{10} A_{ij} + B \log_{10} \left(d_{ij}\right) + C d_{ij} - S_j, \qquad (1)$$

where M_i is the magnitude of the ith earthquake, A_{ij} is the amplitude of earthquake i at station j, d_{ij} is the distance between the hypocenter and the station, B is a parameter related to geometric spreading (B = 1 corresponds to body wave spreading in a homogeneous medium), C is a parameter related to attenuation, and S_j is the station parameter (S_j corresponds to the logarithm of the product of the station gain, including any site effects, and a constant that relates physical amplitude measurements, i.e., pressure or displacement, to the magnitude scale).

[31] Equation (1) can be written as

$$\log_{10} A_{ij} = M_i - B \log_{10} \left(d_{ij}\right) - C d_{ij} + S_j. \qquad (2)$$

Treating M_i, B, C, and S_j as unknowns and calculating d_{ij} for each station event pair, we inverted the resulting linear system of equations for the restricted event set and subsequently used the values of B (1.08 ± 0.13) and C (0.011 ± 0.03) and the S_j to determine magnitudes for the full set. Although no significance should be attached to the values of B and C, the fact that they are reasonable gives confidence in the applicability of equations (1) and (2).

[32] Because there is a trade-off between the average value of the M_i and the average value of the S_j, the absolute magnitudes are unconstrained by this approach and need to be fixed. In order to get at least some idea about absolute magnitudes we made use of two independent approaches. First, we extrapolated the long-term globally registered earthquake activity on this part of the MAR to determine how many events of a certain magnitude would be expected for the duration of our experiment. We then fixed the average magnitude such that the number of recorded events matches the expected number. Second, we measured corner frequencies on the DPG traces for all events in the restricted set, after first correcting for the frequency-dependent response of the instruments. Assuming a stress drop (here 5 bars) and the *Brune* [1970] source model, we can estimate moment magnitudes from the corner frequencies. We then fixed the average magnitude of our estimate, such that magnitudes agree with the moment magnitudes thus estimated. Both approaches involve a number of poorly determined unknowns and uncertain assumptions but agree to within about half a magnitude with each other. We thus consider the reported absolute magnitudes accurate to within 0.5–1 magnitude steps. Relative magnitudes are determined much more reliably with 95% confidence uncertainties of 0.12–0.24 magnitude steps.

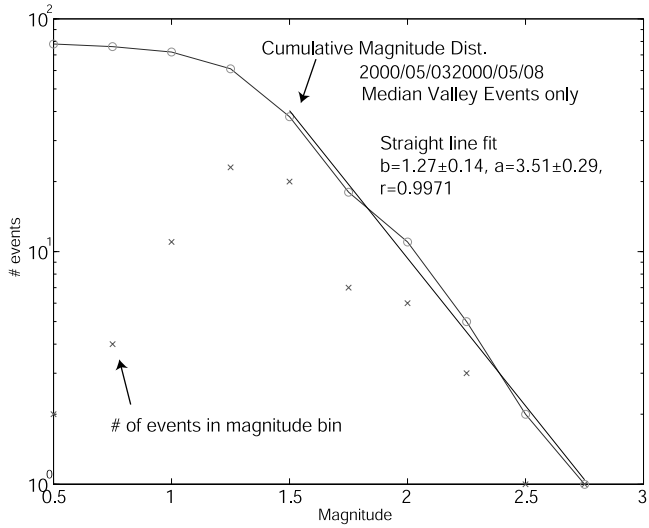

Figure 7. Cumulative magnitude distribution for all median valley events recorded on 3–8 May. Later events were excluded from the b value determination because on those days concurrent shooting, equipment failure, and station pull out noticeably reduced the detection threshold of the array.

[33] We obtained a b value of 1.27 ± 0.14 for the events in the MVSZ (95% confidence error of straight-line fit, Figure 7). The b value is the slope of the cumulative magnitude-frequency distribution and is thus only dependent on relative magnitudes.

[34] Sometimes, b values are quoted for frequency-moment plots with the logarithm of seismic moment as the dependent variable. In order to convert the magnitude b value into a moment b value for easier comparability it is necessary to multiply by a factor of 2/3, yielding b = 0.8 ± 0.1.

5. Refraction Experiment

[35] Four long intersecting wide-angle profiles (up to 170 km long) and three shorter profiles (up to 50 km long) were acquired during the cruise (lines in Figure 1; of the short profiles, only the median valley profile is shown for clarity). Only a brief overview is given here; the data and

analysis were described by *Planert et al.* [2003] and will be presented in more detail elsewhere.

[36] Because of the rough topography the propagation efficiency varied strongly, but in most cases, arrivals can be seen for offsets of more than 40 km, sometimes up to 90 km. Besides crustal phases and mantle phases (P_n), a few Moho reflections (P_mP) are visible in the data. Velocity models were determined by a combination of forward modeling and first-arrival tomographic inversion [*Luetgert*, 1988; *Zelt and Barton*, 1998]. For profiles with sufficient Moho reflections a joint refraction and reflection travel time tomography was employed [*Korenaga et al.*, 2000].

[37] The median valley model is based on a reanalysis of the data shown in Figures 5 and 6 [*Reston et al.*, 2002]. The Moho is found 3–5 km below the seafloor, with the shallowest Moho near the transform fault (Figure 5b). The velocity gradient is fairly uniform between the seafloor ($V_P \sim 3$ km/s) and 2–3 km depth ($V_P \sim 6$ km/s). The lower crustal gradient is then more gentle, with velocities increasing to up to 6.9 km at the Moho, which is underlain by normal-to-low-velocity upper mantle ($V_P \sim 7.5$ km/s). Because of the absence of clear P_mP reflections on the ridge-perpendicular profile, the Moho is not well defined beneath the ICH and the outside corner. By assuming that velocities of $\geq$7.5 km/s are indicative for the upper mantle the models suggest a crustal thickness of 4.0–5.0 km at the eastern flank of the inside corner high and 4.5–5.5 km at the outside corner (Figure 6).

6. Discussion

6.1. Comparison With Teleseismically Recorded Earthquakes

[38] A brief survey as presented here can offer nothing but a snapshot of seismic activity. Nevertheless, we note that the recorded microearthquakes are unlikely to be aftershocks of a large earthquake just before the deployment of the ocean bottom network, as such an event would have been recorded teleseismically. Also, the fact that magnitudes estimated from the corner frequency agree at least in order of magnitude with the rate of events expected from extrapolation of the Gutenberg-Richter curve for events in the global data set for this part of the MAR argues against the possibility that we caught an aftershock or swarm sequence with seismicity rates strongly exceeding long-term averages.

[39] Figure 1 gives an overview of the globally recorded seismicity in the vicinity of the study area. Judging from the apparent location of the strike-slip events in the south of the map, which are presumably all associated with the Ascension transform fault, epicentral mislocation of the Harvard centroid moment tensor (CMT) solutions [*Dziewonski et al.*, 1981] can be as large as 50 km. The events in the *Engdahl et al.* [1998] (EHB) catalog, which were located with short-period body waves, follow the bathymetric trace of the ridge transform faults more closely with formal standard errors of 10–20 km. Only one centroid moment tensor solution locates within the study area. Like the composite focal mechanisms it exhibits (oblique) normal faulting. The dip is ~45° for both nodal planes. Although this is 15–20° steeper than the low-angle plane inferred from the local composite solution, this difference is probably not significant, given the uncertainties inherent in both the local and CMT solutions.

[40] Similar to the results of the ocean bottom survey, the ridge is far more seismically active than the transform. Some earthquakes locate between 5°15′ and 5°30′S, where the median valley was found to be inactive in the ocean bottom survey, but location uncertainties are too large to tell whether these earthquakes were in the median valley or along its flanks.

6.2. Tectonic Interpretation

[41] Within the MVSZ, earthquakes are located predominantly on the western half of the median valley but are fairly uniformly distributed in north-south direction. Whereas some crustal earthquakes have occurred, most of the events have hypocenters beneath the Moho, even when taking into account uncertainties within their location and inaccuracies in the Moho depth, which was obtained by wide-angle modeling. The deepest earthquakes reach a depth of 12 km, or equivalently 8 km beneath the median valley floor. The ridge-parallel cross section along the median valley (Figure 5) suggests an apparent shallowing of the base of the seismogenic zone both toward the volcanic ridge at the segment center and toward the segment end. However, this apparent shallowing is likely to be an artifact of the selection criteria for events with well-constrained depths: the areas around obh03 (near the segment end) and around obh09 (near the southern end of the MVSZ) contain many more events with poorly constrained depths than the region near obh04 (near where the deepest earthquakes are observed).

[42] Uppermost mantle velocities in this section are constrained by the wide-angle data to be larger than 7.5 km/s (Figure 5b). Theoretically, such low velocities would be consistent with up to 20% serpentinization [*O'Reilly et al.*, 1996; *Christensen*, 1966]. In reality, serpentinization is likely to be much weaker as this estimate ignores the effect of the elevated temperatures at the ridge axis (compared to mature oceanic mantle), which can account for most of the velocity reduction. The occurrence of a large number of mantle earthquakes argues further against widespread serpentinization, as even a small degree of serpentinization would weaken mantle peridotite sufficiently to preclude brittle failure [*Escartín et al.*, 1997], whereas mantle stays brittle up to ~750°C [*Wiens and Stein*, 1983].

[43] We now consider the central ridge-perpendicular cross section (Figure 6b). The composite focal solution for this area allows either westward dipping high-angle normal faulting (60° dip) or eastward dipping low-angle normal faulting (30° dip). The surface traces of two faults bounding the MV (F1 on the inside corner side, F2 on the outside corner, Figures 2 and 6) were identified previously from the bathymetric data and, although subdued at the latitude of the cross section, are still identifiable as a step in the bathymetric profile. Whereas the event distribution is clearly incompatible with the pattern expected for a single dominant detachment fault [e.g., *Tucholke and Lin*, 1994], it is not sufficient to uniquely determine the faulting style. At a minimum, two faults are required to be currently active (Figure 6b); these faults would have to be normal and dipping eastward at about 30°. The projection of the inner (eastern) fault would emerge near the surface trace of F1, and no crustal events

Table 2. Comparison of OBS Surveys in the North Atlantic

Area[a]	Reference	Number of Days	Maximum Depth,[b] km	*b* Value ($\log_{10}M_0$)	Number of Events[c] ($M_0 > 10^{19}$ dyn cm)	
					Total	Per Week
22°30′–22°50′N	*Toomey et al.* [1988]	10	8	0.8 ± 0.1(MV floor)	12	8.4
			5	0.5 ± 0.1 (Rift Mountains)		
26°00′–26°13′N	*Kong et al.* [1992]	23		1.0 ± 0.1 (total)	93	28.3
			7	0.6–0.9 ± 0.1 (segment end)		
			6	1.1–1.5 ± 0.1 (segment center)		
28°52′–29°05′N	*Wolfe et al.* [1995] (segment end and ICH only)	41	5.5–7[d]	0.82 ± 0.05	not known	
34°42′–35°00′N	*Barclay et al.* [2001] (segment center only)	43	4	0.94 ± 0.05	4	0.65
35°00′–35°15′N	*Cessaro and Hussong* [1986] (segment end only)	12	9 (14)[e]	0.5–0.7[f]	not known	

[a]The area gives the approximate extent of the area for which the OBS arrays had good coverage.
[b]Depth is quoted relative to the median valley floor.
[c]The number of events above the threshold was determined from the straight-line fits to the frequency log moment curves provided by the references. A threshold of $M_0 > 10^{19}$ dyn cm ($M_w = 1.97$) was chosen because it did not require extrapolation for any of the experiments.
[d]Lower bound is applicable to earthquakes located with at least five OBS; upper bound is applicable to earthquakes located with four OBS.
[e]Larger depth in parentheses is valid only for three isolated events.
[f]Value is derived from duration magnitude *b* value of 0.76–0.99 (the event set includes some transform events).

would have been recorded for the outer (western) fault. Alternatively, faulting distributed through the volume beneath the MV could also produce the observed distribution os seismicity. This faulting could be on either the west or eastward dipping planes, or even both.

[44] Moving on to the southernmost cross section (Figure 6c), we recognize a cluster of events at 9–10 km depth below sea level and two isolated events, one deep, one shallow farther east. Given the short observation time, this pattern is consistent with both faulting along one or two dominant faults (Figure 6c, the slopes of the faulting being suggested by the focal mechanism) or with the recording of a fortuitous subset of events associated with more distributed faulting. Either way, a connection with fault trace F1 seems unlikely, except for the isolated shallow event.

[45] The northernmost section (Figure 6a) presents the most scattered picture, and we do not have a focal solution to guide our interpretation. The three westernmost events probably accommodate diffuse stress within the ICH. Bathymetric structures in and near the MV become more oblique near the transform fault, possibly causing deformation to become more diffuse.

[46] The well-defined volcanic ridge south of 5°16′S [*Reston et al.*, 2002] indicates recent magmatic activity. The ridge coincides with an apparently aseismic zone where earthquakes, if they occur at all, are of much smaller magnitude than those in the MVSZ. During the experiment, only events with a magnitude <1 could have feasibly escaped detection. Although the possibility cannot be excluded that the absence of events is an artifact of the short observational period, the sharpness of the cutoff of seismicity at the southern limit of the MVSZ is nevertheless notable. Elevated temperatures or the presence of fluids could suppress tectonic earthquakes; volcanic earthquakes would be expected to occur but might simply be too small or too intermittent to have been recorded during the experiment. The fact that there is no or only weak shoaling of the base of the seismogenic layer implies that either the temperature gradient along the transition between the MVSZ and the aseismic ridge is large or the transition is controlled by fluids rather than temperature. Seismic velocities could provide further information on the thermal structure, but the median valley refraction profile does not extend far enough south to resolve the velocity structure of the volcanic ridge.

6.3. Synthesis With Previous Microearthquake Surveys

[47] In the following, we contrast our results with those of a number of surveys along the northern MAR at 23°, 26°, 29°, and 35°N (Table 2). The spreading rate of the MAR in this area (2.3 cm/yr) is somewhat slower than at 5°S (3.2 cm/yr), and the plates being separated are different ones [*DeMets et al.*, 1994]. Nevertheless, these surveys represent the closest analogue. The maximum hypocentral depth in this study (8 km below the MV floor) is the same as that observed by *Toomey et al.* [1988] for earthquakes beneath the median valley floor near 23°N, classified as a cold segment by *Thibaud et al.* [1998]. Further similarities are the similar *b* values (0.8 ± 0.1 both at 23°N and in this study, log moment *b* value) and the large cross-axis topographic relief, which characterizes both segments.

[48] The surveys at 23°N [*Kong et al.*, 1992] and 29°N [*Wolfe et al.*, 1995] exhibit slightly lower maximum earthquake depths of 6–7 km below the MV seafloor and have intermediate cross-axis relief. An extreme case is presented by the segment south of the Oceanographer's Transform at 35°N [*Barclay et al.*, 2001], where earthquake depths only reach 4 km below the MV floor, a large moment *b* value of 0.94 is found, and cross-axis relief is small. On the basis of various lines of geophysical evidence, both *Kong et al.* [1992] and *Barclay et al.* [2001] infer recent magmatic injection events for their segments. In spite of the fact that the segment north of the Oceanographer's Transform has been classified as hot by *Thibaud et al.* [1998], *Cessaro and Hussong* [1986] find a low *b* value of 0.7 or less and a fairly uniform depth distribution between 2 and 9 km depth below the MV floor, with three events apparently at depths of 12–14 km near the transform-ridge intersection. However, the focal mechanisms of some of their events hint that are they responding to stresses associated with the ridge-transform intersection rather than effecting ridge-normal extension.

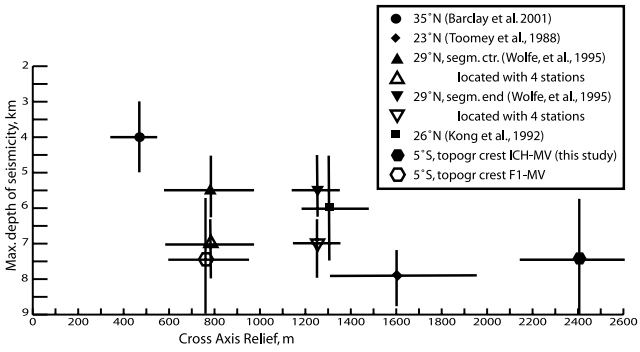

Figure 8. Maximum depth of seismicity versus cross-axis relief. Adapted from *Barclay et al.* [2001] with the results of this study added. Cross-axis relief was determined by averaging the relief from the median valley floor to the first crest of the sidewall, with the error bars representing the variability of the relief thus measured among several parallel profiles in the vicinity of the hypocenters. For the present study, there is an ambiguity whether the crest of fault F1 or the inside corner high should be used, so both alternatives are presented. The error bars for the maximum earthquake depths are determined from the error bars of the deepest events in the survey. At 29°N, maximum inferred earthquake depths differ depending whether events located with only four stations are included in the estimate (solid triangles) or at least five stations were required (open symbols).

[49] On the basis of body waveform modeling of teleseismically earthquakes, *Huang and Solomon* [1988] inferred a maximum centroid depth of 3–3.5 km below the MV floor for ridge earthquakes at a full spreading rate of 3 cm/yr. Assuming uniform slip and rigidity, this centroid depth implies a seismogenic zone twice as thick, i.e., 6–7 km, only slightly less than the depth indicated by microearthquakes.

[50] *Barclay et al.* [2001] pointed out an apparent correlation between large cross-axis relief and large maximum earthquake depth (Figure 8). The segment presented in this work follows this pattern, but if the topographic relief is measured from the median valley to the crest of the ICH ridge, the maximum depth saturates at 8 km (below the MV floor). There also appears to be an inverse correlation between the maximum earthquake depth and the *b* value with large *b* values being associated with shallow maximum depths (Table 2 and this study), although there is at least one exception to this rule (rift mountains at 23°N). Physically, such a correlation is not surprising, as increased temperatures would lift the base of the seismogenic layer as well as increase the *b* value.

[51] Marked differences also exist in the style of faulting inferred for the various segments. *Kong et al.* [1992] attribute most seismic activity to accommodation of cooling stresses induced by an already solidified but still hot igneous intrusion. For the other segments, primarily tectonic extension is invoked. *Barclay et al.* [2001] interpret the earthquakes near the segment center to result from stress on normal faults bounding the valley in accordance with classic extension along segment centers of slow spreading ridges [*Mutter and Karson*, 1992]. Similar to our interpretation of the seismicity at 5°S, *Toomey et al.* [1988] infer a large mantle-penetrating normal fault for the segment at 29°N, albeit at a dip of 45°N. In contrast to the rather weak seismicity underneath the ICH in this experiment the ICH was the most seismically active area in the microearthquake survey at 29°N [*Wolfe et al.*, 1995]. The ICH events occurred at depths between 3 and 6 km (relative to the median valley seafloor), placing most of them in the mantle as gravity data indicate a thin crust underneath the ICH. *Wolfe et al.* [1995] interpreted these ICH events as accommodating extension over a broad area rather than along a well-defined detachment as required by the *Tucholke and Lin* [1994] model. Alternatively, the events could be associated with successor faults that accommodate flexing of an exhumed core complex. We prefer the original interpretation because there is no evidence for a large seismically active detachment surface along the western wall of the MV: a composite focal mechanism shows normal faulting with a 45° dip, but the microearthquakes do not line up along a corresponding surface. Intriguingly, the segments at 5°S and at 29°N also present rather different morphologies (Figure 9), which

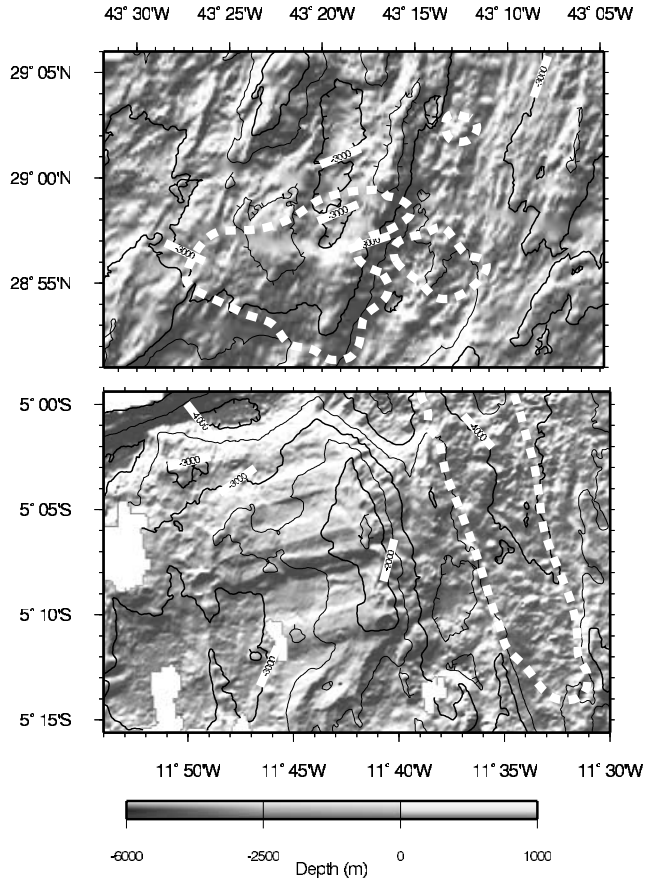

Figure 9. Detail of the bathymetry of the ICHs of the ridge segments at 29°N (top, *Wolfe et al.* [1995]) and 5°S (bottom, this study). Both data sets are plotted at the same scale and using the same gray scale; illumination is from NNW in both images, but intensity normalization has been optimized for each image separately to enhance contrast. The resolution of the top image is 200 m, and that of the bottom image is 100 m. Dashed white lines delineate the most seismically active zones.

reflect the differences in seismicity. The ICH at 5°S is characterized by pronounced axis-perpendicular striations and large topographic relief. In contrast, the ICH at 29°N has a rough and rugged surface but lacks well-defined striations and has less relief. We have to remember that the striations at 5°S are not related to the currently active faults but record an earlier phase of extension before the proposed ridge jump. Although it is possible and even likely that over time the faults at 5°S will exhume their footwalls, there is currently no need to accommodate bending of an exhumed IC complex or additional extension within the ICH region, so that the low seismic activity is not surprising. This observation raises the question what controls the style of extension that a particular ridge adopts. We note that the ICH at 29°N is located next to a nontransform discontinuity, whereas the one at 5°S is next to a 70 km offset transform. However, an earlier microearthquake OBS survey near major transforms also reported diffuse microearthquake activity at the inside corner (Vema Transform, 11°N [*Rowlett and Forsyth*, 1984]; Oceanographer's Transform, 35°N [*Cessaro and Hussong*, 1986]), so the question is open.

7. Conclusion

[52] During a 10 day passive ocean bottom survey of the MAR just south of the 5°S fracture zone we observed seismic activity to be concentrated in the western half of the median valley, termed the median valley seismic zone (MVSZ). In axis-parallel direction the MVSZ is bounded by the transform fault to the north and the axial volcanic ridge to the south. A few scattered events occurred on the transform fault, below the ICH and beneath the western side wall of the median valley at the latitude of the volcanic ridge. The maximum earthquake depth (8 km below the median valley floor) and moment *b* values (0.8) in the MVSZ, as well as the large cross-axis relief, are typical for a ''cold'' segment. The depth distribution of earthquakes indicates that tectonic extension is accommodated along mantle-penetrating normal faults. Seismic activity in the mantle and only moderately low velocities beneath the Moho preclude a large degree of serpentinization there. The presence of a well-defined volcanic ridge and the absence of recorded earthquakes near the segment center indicate that it might be hot and magmatically active. This contrast between segment center and segment end is expected, but the transition appears to be surprisingly sharp, with no or little shoaling of earthquake depths or reduction of seismic activity on approaching the aseismic zone.

[53] **Acknowledgments.** The R/V *Meteor* cruise M47/2 and subsequent data analysis was funded by the Deutsche Forschungsgemeinschaft. Special thanks goes to Capt. Martin Kull and his crew for their excellent support during the cruise and the scientific shipboard party for collecting the data. We thank Anne Otto for carrying out most of the initial event checking and picking. Comments by Douglas Toomey and an anonymous reviewer and Associate Editor helped to focus and clarify the paper. Software packages contributing substantially to the analysis, processing and presentation of this data set were GMT [*Wessel and Smith*, 1991], SeisAn [*Havskov and Ottemöller*, 1999], and the PASSCAL suite of programs; part of the trigger program was provided by William Langin. Additional bathymetric data for Figure 9 were obtained from the Ridge Multi Beam Synthesis Project at Lamont-Doherty Earth Observatory (http://data.ridge2000.org/bathy/). This is Cambridge Department of Earth Sciences contribution 7790.

References

Barclay, A. H., D. R. Toomey, and S. C. Solomon (2001), Microearthquake characteristics and crustal V_P/V_S structure at the Mid-Atlantic Ridge, 35°N, *J. Geophys. Res.*, *106*, 2017–2034.

Brune, J. (1970), Tectonic stress and the spectra of seismic shear waves from earthquakes, *J. Geophys. Res.*, *75*, 4997–5009.

Cessaro, R. K., and D. M. Hussong (1986), Transform seismicity at the intersection of the Oceanographer Fracture Zone and the Mid-Atlantic Ridge, *J. Geophys. Res.*, *91*, 4839–4853.

Christensen, N. I. (1966), Elasticity of ultrabasic rocks, *J. Geophys. Res.*, *71*, 5921–5932.

DeMets, C., R. Gordon, D. F. Argus, and S. Stein (1990), Current plate motions, *Geophys. J. Int.*, *101*, 425–478.

DeMets, C., R. Gordon, D. F. Argus, and S. Stein (1994), Effect of recent revisions to the geomagnetic reversal time scale on estimates of current plate motions, *Geophys. Res. Lett.*, *21*, 2191–2194.

Dziewonski, A. M., T.-A. Chou, and J. H. Woodhouse (1981), Determination of earthquake source parameters from wavefrom data for studies of global and regional seismicity, *J. Geophys. Res.*, *86*, 2825–2852.

Engdahl, E., R. D. van der Hilst, and R. P. Buland (1998), Global teleseismic earthquake relocation with improved travel times and procedures for depth determination, *Bul. Seismol. Soc. Am.*, *88*, 722–743.

Escartín, J., and J. Lin (1995), Ridge offsets, normal faulting, and gravity anomalies of slow spreading ridges, *J. Geophys. Res.*, *100*, 6163–6178.

Escartín, J., G. Hirth, and B. Evans (1997), Nondilatant brittle deformation of serpentinites: Implications for Mohr-Coulomb theory and the strength of faults, *J. Geophys. Res.*, *102*, 2897–2913.

Havskov, J., and L. Ottemöller (1999), SeisAn Earthquake Analysis Software, *Seismol. Res. Lett.*, *70*, 532–534.

Huang, P. Y., and C. S. Solomon (1988), Centroid depths of mid-ocean ridge earthquakes: Dependence on spreading rate, *J. Geophys. Res.*, *93*, 13,445–13,477.

Hutton, L. K., and D. Boore (1987), The m_l scale in southern california, *Bul. Seismol. Soc. Am.*, *77*, 2074–2094.

Kissling, E. W., W. L. Ellsworth, D. Eberhard-Philipps, and U. Kradolfer (1994), Initial reference model in local earthquake tomography, *J. Geophys. Res.*, *99*, 19,636–19,646.

Kong, L. S. L., S. C. Solomon, and G. M. Purdy (1992), Microearthquake characteristics of a mid-ocean ridge along-axis high, *J. Geophys. Res.*, *97*, 1659–1685.

Korenaga, J., W. S. Holbrook, G. M. Kent, P. B. Kelemen, R. S. Detrick, H.-C. Larsen, J. R. Hopper, and T. Dahl-Jensen (2000), Crustal structure of the southeast Greenland margin from joint refration and reflection seismic tomography, *J. Geophys. Res.*, *105*, 21,591–21,614.

Luetgert, J. H. (1988), User's manual for RAY84/R83PLT—Interactive two-dimensional raytracing/synthetic seismogram package, *U. S. Geol. Surv. Open File Rep., 88-238*.

Mutter, J. C., and J. A. Karson (1992), Structural processes at slow-spreading ridges, *Science*, *257*, 627–634.

Neumann, G. A., and D. W. Forsyth (1993), The paradox of the axial profile: Isostatic compensation along the axis of the Mid-Atlantic Ridge?, *J. Geophys. Res.*, *98*, 17,891–17,910.

O'Reilly, B. M., F. Hauser, A. W. B. Jacob, and P. M. Shannon (1996), The lithosphere below the Rockall Trough: Wide-angle seismic evidence for extensive serpentinisation, *Tectonophysics*, *255*, 1–23.

Planert, L., F. Tilmann, W. Weinrebe, E. Flueh, and T. Reston (2003), A wide-angle survey of the Mid-Atlantic Ridge at 5°S, *Eos Trans. AGU*, *84*(46), Fall Meet. Suppl., Abstract T12D-0493.

Reston, T., W. Weinrebe, I. Grevemeyer, E. R. Flueh, N. C. Mitchell, L. Kirstein, C. Kopp, H. Kopp, and participants of Meteor 47/2 (2002), A rifted inside corner massif on the Mid-Atlantic Ridge at 5°S, *Earth Planet. Sci. Lett.*, *200*, 255–269.

Rowlett, H., and F. W. Forsyth (1984), Recent faulting and microearthquakes at the intersection of the Vema Fracture Zone and the Mid-Atlantic Ridge, *J. Geophys. Res.*, *89*, 6079–6094.

Rundquist, D. V., and P. O. Sobolev (2002), Seismicity of mid-oceanic ridges and its geodynamic implications: A review, *Earth Sci. Rev.*, *58*, 143–151.

Shaw, P. R., and J. Lin (1993), Causes and consequences of variations in faulting style at the Mid-Atlantic Ridge, *J. Geophys. Res.*, *98*, 21,839–21,851.

Smith, D. K., J. Escartín, M. Cannat, M. Tolstoy, C. G. Fox, D. R. Bohnenstiehl, and S. Bazin (2003), Spatial and temporal distribution of seismicity along the northern Mid-Atlantic Ridge (15°–35°N), *J. Geophys. Res.*, *108*(B3), 2167, doi:10.1029/2002JB001964.

Smith, W. H. F., and D. T. Sandwell (1997), Global sea floor topography from satellite altimetry and ship depth soundings, *Science*, *277*, 1956–1962.

Thibaud, R. P., P. Gente, and M. Maia (1998), A systematic analysis of the Mid-Atlantic Ridge morphology and gravity between 15°N and 40°N, *J. Geophys. Res.*, *103*, 24,223–24,243.

Toomey, D. R., S. C. Solomon, G. M. Purdy, and M. H. Murray (1988), Microearthquakes beneath the median valley of Mid-Atlantic Ridge near 23°N: Tomography and tectonics, *J. Geophys. Res.*, *93*, 9063–9112.

Tucholke, B. E., and J. Lin (1994), A geological model for the structure of ridge segments in slow spreading ocean crust, *J. Geophys. Res.*, *99*, 11,937–11,958.

Waldhauser, F., and W. L. Ellsworth (2000), A double-difference earthquake location algorithm, *Bul. Seismol. Soc. Am.*, *90*, 1353–1368.

Wessel, P., and W. H. F. Smith (1991), Free software helps map and display data, *Eos Trans. AGU*, *72*, 441, 445–446.

Wiens, D. A., and S. Stein (1983), Age dependence of oceanic intraplate seismicity and implications for lithospheric evolution, *J. Geophys. Res.*, *88*, 6455–6468.

Wilcock, W. S. D., and D. R. Toomey (1991), Estimating hypocentral uncertainties for marine earthquake surveys: A comparison of the generalized inverse and grid search methods, *Mar. Geophys. Res.*, *13*, 161–171.

Wolfe, C. J., G. M. Purdy, D. R. Toomey, and S. C. Solomon (1995), Microearthquake characteristics and crustal velocity structure at 29°N on the Mid-Atlantic Ridge: The architecture of a slow spreading segment, *J. Geophys. Res.*, *100*, 24,449–24,472.

Zelt, C., and P. Barton (1998), Three-dimensional seismic refraction tomography: A comparison of two methods applied to data from the Faeroe Basin, *J. Geophys. Res.*, *103*, 7187–7210.

E. Flueh, L. Planert, T. Reston, and W. Weinrebe, IFM-GEOMAR, Wischofstr. 1-3, D-24148 Kiel, Germany. (eflueh@ifm-geomar.de; lplanert@ifm-geomar.de; treston@ifm-geomar.de; wweinreb@ifm-geomar.de)

F. Tilmann, Bullard Laboratories, Department of Earth Sciences, University of Cambridge, Madingley Rise, Madingley Road, Cambridge CB3 0EZ, UK. (tilmann@esc.cam.ac.uk)

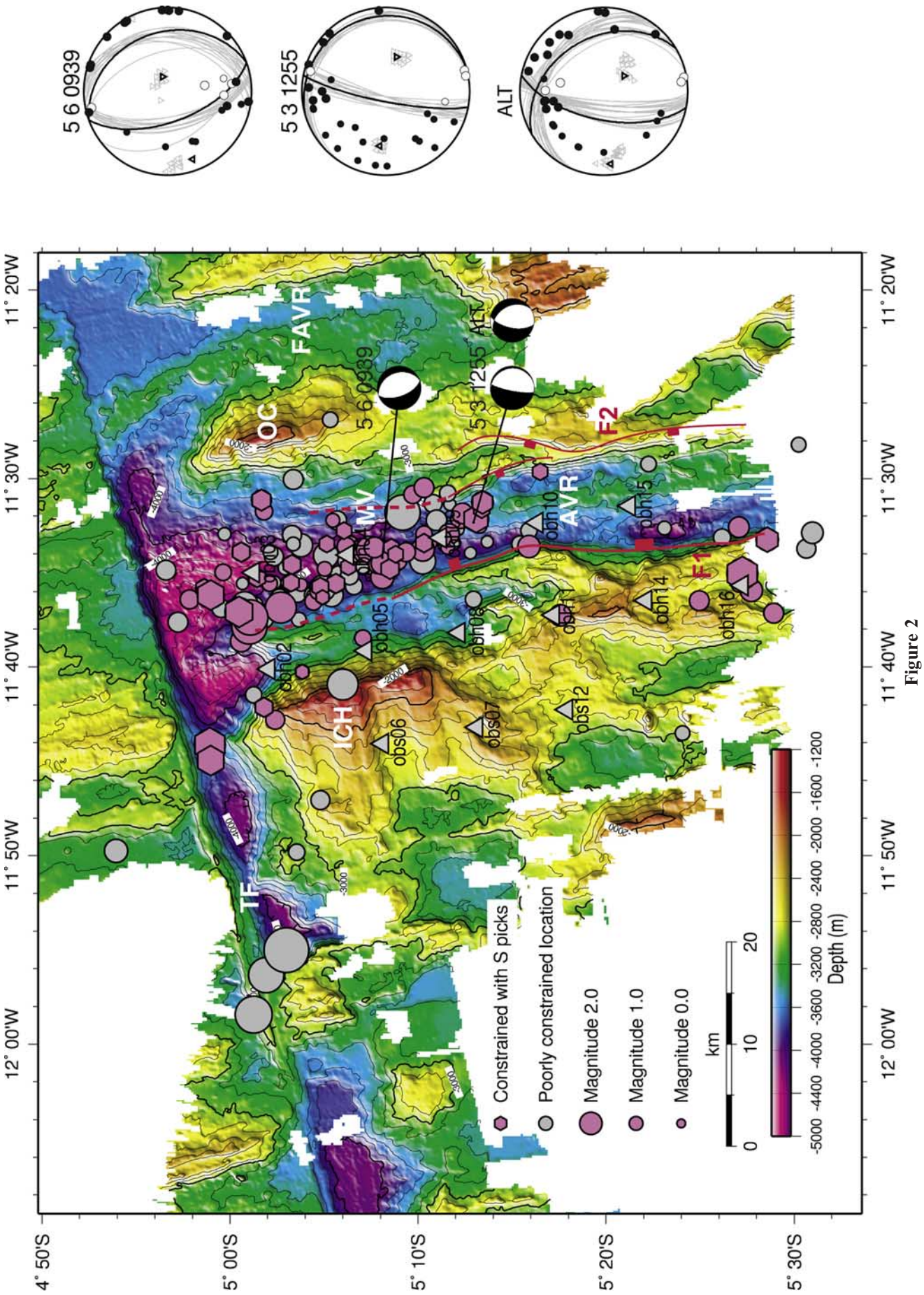
5 6 0939
5 3 1255
ALT
11° 20'W
11° 30'W
11° 40'W
11° 50'W
12° 00'W
4° 50'S
5° 00'S
5° 10'S
5° 20'S
5° 30'S
OC
FAVR
MV
AVR
ICH
TF
F1
F2
obs06
obs07
obs12
obn02
obn05
obn06
obn10
obn11
obn14
obn15
obn16
Constrained with S picks
Poorly constrained location
Magnitude 2.0
Magnitude 1.0
Magnitude 0.0
km
0
10
20
Depth (m)
-5000 -4400 -4000 -3600 -3200 -2800 -2400 -2000 -1600 -1200

Figure 2

Figure 2. Distribution of earthquakes recorded with the ocean bottom stations. Red circles and hexagons are events located with at least five stations and azimuthal gap <300°; hexagons indicates at least one *S* arrival was used. Gray circles are marginally located events not fulfilling above criteria. Gray triangles are station locations. Composite focal mechanisms for two groups of events are shown as lower hemisphere projections. For event 5 3 1255 an alternative solution (labeled ALT), which results from the use of a different velocity model, is also shown. Details of the focal mechanism solutions are shown to the right of the map, where the thick black line shows the preferred solution (identical to the mechanisms shown in the map), the thin gray lines indicate other solutions that are consistent with the data, and black and white circles show compressive and dilatational first motion, respectively. Direct rays leaving the earthquake focus in upward direction are plotted at the opposite azimuth, and the incidence angle is set to the angle between the ray direction and vertical up. Triangles indicate possible *P* and *T* axes. The bathymetry is based on processed multibeam soundings acquired during the cruise. Marked morphological features: MV, Median Valley; TF, transform fault; ICH, inside corner high; OC, outside corner massif; AVR, axial volcanic ridge; FAVR, extinct (fossil) axial volcanic ridge. Faults F1 and F2 were identified by [*Reston et al.*, 2002]. The dashed lines show possible continuations of the faults where their morphological expression is less clear.